Check for updates

Tailoring the Charge/Discharge Potentials and Electrochemical Performance of SnO$_2$ Lithium-Ion Anodes by Transition Metal Co-Doping

Adele Birrozzi,[a, b] Jakob Asenbauer,[a, b] Thomas E. Ashton,[c] Alexandra R. Groves,[c] Dorin Geiger,[d] Ute Kaiser,[d] Jawwad A. Darr,[c] and Dominic Bresser*[a, b]

It has been shown that the introduction of several transition metal (TM) dopants into SnO$_2$ lithium-ion battery anodes can overcome the issues associated with the irreversible capacity loss from the conversion reaction of SnO$_2$ and the aggregation of the metallic Sn particles formed upon lithiation. As the choice of the single dopant, however, plays a decisive role for the achievable energy density – precisely its redox potential – we investigate herein TM co-doped SnO$_2$, prepared by using a readily scalable continuous hydrothermal flow synthesis (CHFS) process, to tailor the dis-/charge profile and by this the energy density. It is shown that the judicious choice of different elemental doping combinations in samples made via CHFS simultaneously improves the cycling performance and the full-cell energy density. To support these findings, we realized a lithium-ion full-cell incorporating the best performing co-doped SnO$_2$ as negative electrode and high-voltage LiNi$_{0.5}$Mn$_{1.5}$O$_4$ (LNMO) as positive electrode–to the best of our knowledge, the first full-cell based on such anode material in combination with LNMO as cathode active material.

1. Introduction

Lithium-ion batteries (LIBs) are still the first choice for electro-chemical energy storage applications, though further improvement is required concerning their energy and power density – in particular for large-scale applications such as (hybrid) electric vehicles.[1–3] Since performance characteristics are essentially driven by the cell chemistry, huge efforts have been made to identify and develop alternative electrode active materials. Particularly, the replacement of graphite anodes (which have an intrinsically limited charge rate) is a challenge, though this, if overcome, would enhance the power density.[4–6] In addition, energy density is limited for such anodes since the theoretical maximum capacity of graphite (372 mAh g^{-1}) has essentially

been achieved in commercial LIBs. When looking for potential alternatives to graphite, researchers have largely focused on two different material classes: (i) Metals and metalloids such as Si, Sn, Zn, which can reversibly alloy with lithium electrochemically[7] and (ii) conversion compounds as transition metal (TM) oxides, which reversibly form the metallic TM and Li$_2$O.[8–11] These material classes, however, suffer intrinsic challenges including extensive volume variation and large voltage hysteresis during cycling, for alloying and conversion materials, respectively. In order to overcome these challenges, dual conversion and alloying materials (CAMs) have been proposed.[11] These alternative anodes combine both charge storage mechanisms in one single material. One representative CAM, with theoretical capacities of almost 1500 mAh g^{-1}, is transition metal doped tin oxide,[12–17] for which the choice of the incorporated transition metal (and its redox potential) plays a key role for achieving high energy density and long-term stable cycling.[16–19]

Herein, we have developed electroactive TM co-doped SnO$_2$ to achieve enhanced electrochemical performance. The continuous hydrothermal flow synthesis (CHFS) method[20] was chosen as a reproducible and scalable process for the production of co-doped tin oxide nanoparticles. The introduction of more than one TM dopant allows for tailoring the dis-/charge potentials and thus a combination of simultaneous high energy density (at the full-cell level), high cycling stability, and good rate capability. The careful electrochemical investigation of a series of co-doped samples provides insight into the effect of the dopants and is expected to contribute to some general guidelines for the further development of advanced CAMs in the future. Finally, we realized a lithium-ion full-cell with the best performing co-doped SnO$_2$ as negative electrode active material and high-voltage LiNi$_{0.5}$Mn$_{1.5}$O$_4$ (LNMO) as positive

[a] A. Birrozzi, J. Asenbauer, Dr. D. Bresser
Helmholtz Institute Ulm (HIU),
89081 Ulm, Germany

[b] A. Birrozzi, J. Asenbauer, Dr. D. Bresser
Karlsruhe Institute of Technology (KIT),
76021 Karlsruhe, Germany
E-mail: dominic.bresser@kit.edu

[c] Dr. T. E. Ashton, A. R. Groves, Prof. J. A. Darr
University College London (UCL), Department of Chemistry,
London WC1H 0AJ, United Kingdom

[d] Dr. D. Geiger, Prof. U. Kaiser
Ulm University, Central Facility for Electron Microscopy,
89081 Ulm, Germany

electrode material to support our findings obtained for the half-cell studies.

2. Result and Discussion

2.1. Structural and Morphological Characterization

Materials synthesis was conducted by means of CHFS as readily scalable and fast synthesis method. The general process is shown in a simplified flow diagram in Figure 1a. All the samples obtained, which showed different colors depending on the incorporated dopants (see Figure S1), were characterized by X-ray diffraction (XRD) and transmission electron microscopy (TEM). The XRD data is presented in Figure S2 and Figure 1b for the mono-doped and co-doped SnO_2 samples, respectively. In both cases, the XRD data for pure SnO_2 is shown as a comparison. All diffractograms show good agreement to the SnO_2 reference (PDF 01-070-6995) for a tetragonal rutile structured tin oxide, space group $P42/mnm$, apart from a reversed intensity ratio for the {110} and {101} reflections, indicating an anisotropic crystallite growth along the latter direction. The absence of any additional reflections demonstrates that all the materials were phase-pure and that the TM dopants had been successfully introduced into the SnO_2 crystal structure.[12,15,16] The rather broad reflections indicate small crystalline domains common in nanoparticulate powders, while the general peak intensity ratio follows basically the same trend in all cases, suggesting a similar particle shape.

These findings were confirmed by the TEM micrographs for pure SnO_2 and TM co-doped SnO_2 shown in Figure 1c, revealing rod-like nanoparticles with a diameter of less than 10 nm, while the length varies slightly with the dopants used. Generally, the presence of the dopants, confirmed by EDX analysis, results in an elongated, anisotropic shape, especially so for SCFMO. The determination of the specific surface area, calculated by means of the Brunauer-Emmett-Teller (BET) method, revealed comparable values for SnO_2 (ca. 93 $m^2 g^{-1}$, serving as reference) and SCMO (ca. 99 $m^2 g^{-1}$, serving as example for the (co-)doped samples). This is in good agreement with the XRD and TEM results, which do not show substantial differences among the samples.

2.2. Optimizing the Dopant Combination

After the initial structural and morphological characterization of the materials, we focused on their electrochemical characterization. Firstly, cyclic voltammetry (CV) was performed to investigate the influence of the presence of more than one dopant on the de-/lithiation behavior. The results for SCMO, SCFO, SFMO, and SCFMO are presented in Figure 2a, including the performance for pure SnO_2 as a reference. In the negative sweep for the doped samples, the first reduction peak at ca. 0.9 V (assigned as A in Figure 2a) is attributed to the conversion reaction of (TM co-doped) SnO_2 to metallic tin (and the corresponding metallic TMs) accompanied by the formation of Li_2O.[16] Remarkably, this peak is shifted towards higher potentials for the TM co-doped samples, presumably due to a
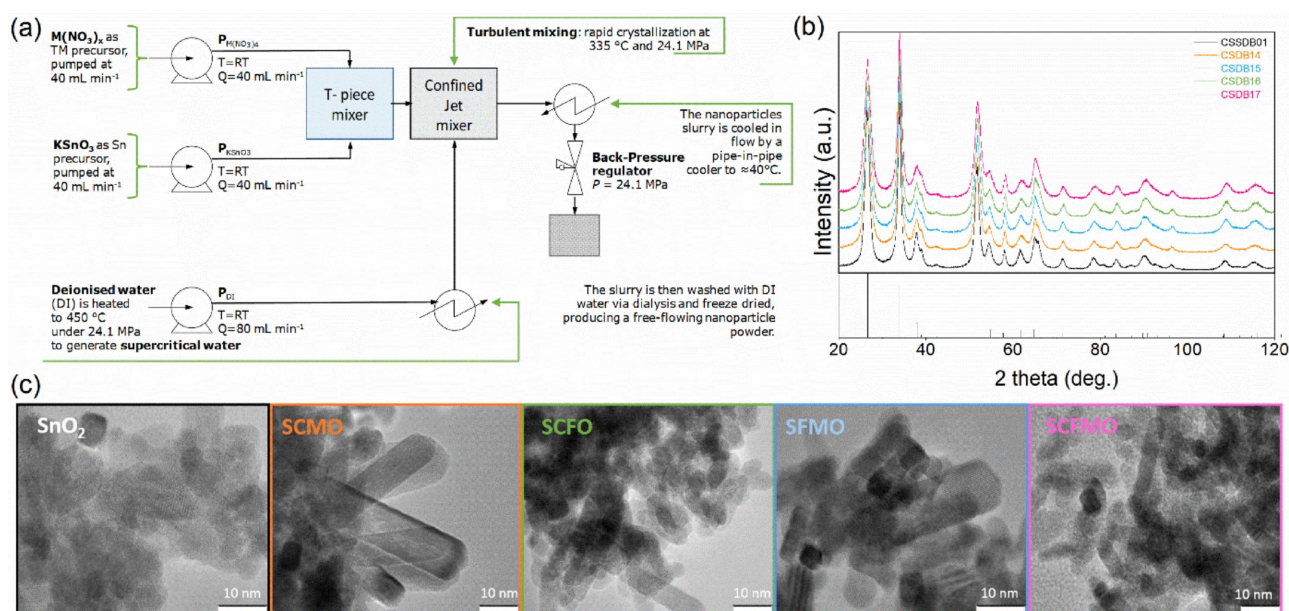

Figure 1. (a) Scheme of the CHFS apparatus. From A and B, the metal precursor solutions are pumped in the confined jet mixer. From C, water is supplied through an electric heater to form supercritical water. Subsequently, there is a cooling step and the desired material can be collected after a back-pressure regulator. (b) Diffractograms of the synthesized materials; from bottom to top: Pure SnO_2 (in black), $Sn_{0.9}Co_{0.05}Mn_{0.05}O_2$ (SCMO, in orange), $Sn_{0.9}Co_{0.05}Fe_{0.05}O_2$ (SCFO, in blue), $Sn_{0.9}Fe_{0.05}Mn_{0.05}O_2$ (SFMO, in green), and $Sn_{0.85}Co_{0.05}Fe_{0.05}Mn_{0.05}O_2$ (SCFMO in pink). In the bottom, the reference pattern from cassiterite SnO_2 is shown (PDF 01-070-6995). (c) TEM micrographs (from left to right) for pure SnO_2 (in black), SCMO (in orange), SCFO (in green), SFMO (in blue), and SCFMO (in pink).
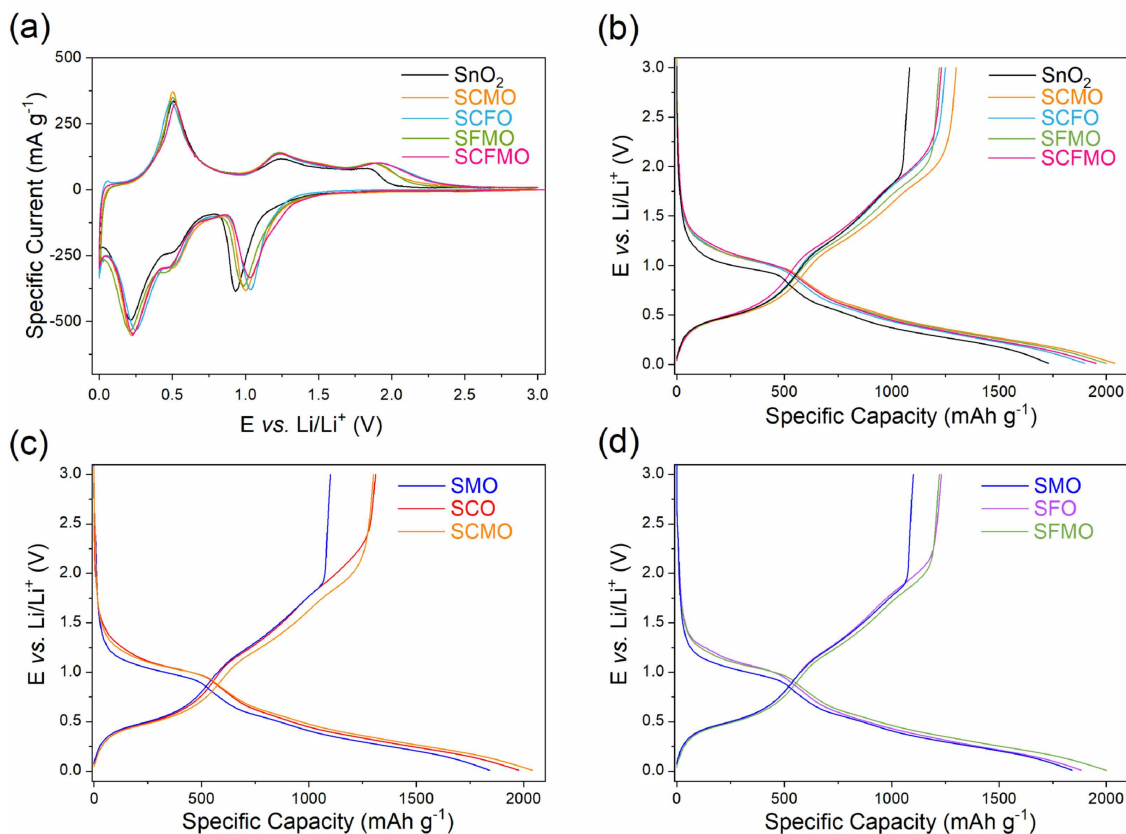
Figure 2. (a) Cyclic voltammograms for electrodes based on SnO_2, SCMO, SCFO, SFMO, and SCFMO recorded for potential range from 0.01 to 3.0 V with a scan rate of 50 µV s^{-1}. (b-d) Comparison of the 1st cycle galvanostatic dis-/charge profiles for (b) TM co-doped SnO_2 (SCMO in orange, SCFO in blue, SFMO in green, and SCFMO in pink) including pure SnO_2 (in black) as reference, (c) mono-doped SMO (in blue), SCO (in red), and co-doped SCMO (in orange), as well as (d) mono-doped SMO (in blue), SFO (in purple), and co-doped SFMO (in green). Specific current: 20 mA g^{-1}.

relatively higher redox potential of the dopant compared to tin in the given electrochemical setup. This shift is especially pronounced for the co-doped SnO_2 containing Fe and/or Co as a result of the relatively higher redox potential compared to manganese (e.g., Fe$^{2+/0}$: −0.44 V; Co$^{2+/0}$: −0.28 V; Mn$^{2+/0}$: −1.18 V; all referring to the SHE in aqueous electrolytes). Generally, the presence of the dopants results in a mixed reduction potential for the dopants and tin and a reduction in polarization potentially due to increased electronic conductivity for the materials.[16] The following peaks, a relatively smaller shoulder at around 0.5 V and an intense peak at 0.2 V (labelled as B and C, respectively, in Figure 2a), have been assigned to the alloying reaction of tin and lithium *via* multiple steps towards the formation of Li$_x$Sn ($0 < x \leq 4.4$).[16] Comparing the CV peaks for the different samples shows that the evolving current is greater for the TM co-doped tin oxide samples compared to pure SnO_2, indicating extended lithiation, i.e., lithium storage capacity, as a result of the higher electronic conductivity in presence of the metallic TMs. The CV peak for the electrolyte decomposition, commonly expected at ca. 0.8 V,[21] is not observed-presumably due to an overlap with peak A. For the subsequent positive sweep, the peak at ca. 0.5 V (labelled D in Figure 2a) represents the dealloying process, while the reoxidation and backformation of Li$_2$O takes

place at ca. 1.22 V and 1.8 V (peaks labelled E and F, respectively, in Figure 2a).[16] The effect of the TM dopants becomes especially visible when comparing feature F. The maximum intensity is significantly shifted towards higher potentials, especially for the manganese-free sample SCFO and the relatively manganese-poor sample SCFMO, with an increased current flow observed above 1.8 V. This finding is in excellent agreement with a previous study on the impact of the different TM dopants by some of the authors.[16] The general shift to higher potentials and increased current flow has been assigned to the enhanced reconversion reaction in the presence of the TM dopant(s). This shift is particularly pronounced for those samples comprising Fe and/or Co due to the relatively higher oxidation potentials of Fe and Co,[16] as demonstrated by the comparison of 1st cycle galvanostatic dis-/charge profiles for mono-doped SnO_2 samples presented in Figure S3 (see also the corresponding discussion). Focusing on the effect of the TM co-doping, a comparison of the 1st cycle galvanostatic dis-/charge profiles is presented in Figure 2b–d. Whilst all co-doped samples show a higher onset potential for the reduction reaction compared to non-doped SnO_2 (Figure 2b; in line with the CV results), the subsequent reoxidation reveals that the presence of two or more dopants provides a synergetic effect. In fact, sample SFMO (with no Co) has the

lowest potential at which the reoxidation is completed, while manganese-free SCFO shows the highest potential (together with SCFMO). Therefore, in these samples the dopants Co and Fe dominate the de-/lithiation behavior. Notably, particularly high synergy is observed for the simultaneous doping of manganese and cobalt (Figure 2c) or manganese and iron (Figure 2d) which results in lower potentials for completion of the oxidation (delithiation) reaction compared to mono-doped SFO and SCO, while simultaneously maintaining the relatively higher capacity compared to mono-doped SMO (see also Figure S3 for a comparison of the different mono-doped samples).

To further characterize the impact of the co-doping on the electrochemical performance, we conducted rate capability studies with different anodic cut-off potentials (3.0, 2.0, and 1.1 V), keeping in mind also the potential practical application of these materials, for which anodic cut-off potentials as high as 3.0 V are of limited relevance. As shown in Figure S4 for SCMO, limiting the anodic cut-off potential to 1.1 V substantially enhances the cycling stability, whilst limiting it to 2.0 V shows no substantial improvement compared to an anodic cut-off of 3.0 V. This enhanced cycling stability, accompanied by increased capacities at very high currents of 2.0 and 5.0 A g^{-1}, has been assigned to relatively smaller volume changes and less structural reorganization within the active material due to the focus on the alloying reaction and a reduced contribution of the conversion reaction, while maintaining an extensive percolating electronically conductive network of the metallic TM nanograins. In fact, comparing the capacity reversibly obtained at 0.1 A g^{-1}, i.e., ca. 640 mAh g^{-1}, with the theoretical maximum of about 734 mAh g^{-1} for Li$_{4.4}$Sn, indicates that also the alloying reaction remains incomplete with such anodic cut-off potential – presumably due to a lack of electronic conductivity, as a similar experiment (i.e., capacity-limited cycling with a comparable anodic cut-off) for carbon-coated

Sn$_{0.9}$Fe$_{0.1}$O$_2$ provided capacities exceeding the theoretical maximum for the alloying reaction.[12]

Figure 3a presents the summary of the rate test data for all co-doped samples. Interestingly, the manganese-containing samples outperform manganese-free SCFO electrodes at high currents, indicating that Mn plays a critical role for the rate capability of TM co-doped SnO$_2$. Generally, however, the capacity loss at elevated currents is reduced for all samples when limiting the upper cut-off potential to 1.1 V. The impact of the anodic cut-off potential is comparatively shown also in Figure 3b, assuming a theoretical full-cell with LiNi$_{0.5}$Mn$_{1.5}$O$_4$ (LNMO) serving as cathode characterized by a working voltage of 4.7 V vs. Li/Li$^+$ and a specific capacity of 140 mAh g^{-1}. This comparison reveals three main points: Firstly, limitation of the anodic cut-off potential has a substantially positive impact on the achievable energy density (due to less active material required on the cathode side). Secondly, SCMO greatly outperforms the other co-doped samples (in line with the previous results), and, thirdly, SCMO/LNMO lithium-ion full-cells could provide an energy density of 475 Wh kg^{-1} on the active material level (if the initial capacity loss can be addressed).

2.3. Comparison of Carbon-coated SCMO@C and SnO$_2$@C: Impact of the Dopants

Due to the above results, the most promising sample SCMO was chosen for further investigation. With the aim of further improving its cycling performance, a carbonaceous coating was applied to the as-synthesized sample. Thermogravimetric analysis (TGA) of the coated sample revealed that the carbon content was ca. 16 wt% – just like for the carbon-coated non-doped SnO$_2$@C serving as reference for a direct comparison with carbon-coated SCMO@C in order to differentiate between the impact of the carbon coating and the Co/Mn co-doping.
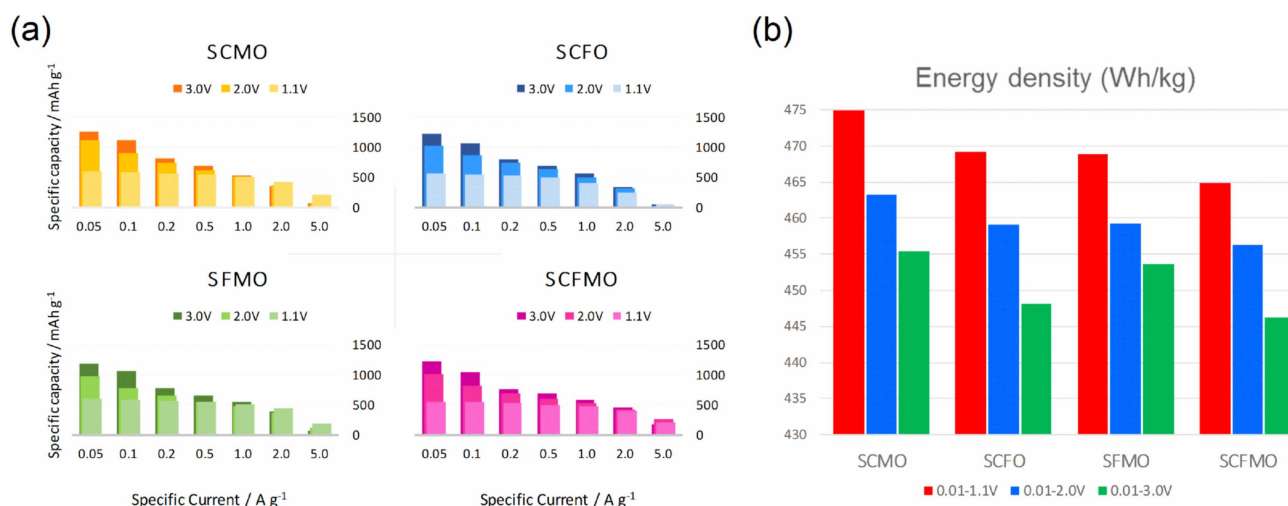

Figure 3. (a) Summary of the specific capacity obtained at varying specific currents and anodic cut-off potentials for all co-doped samples and (b) energy density of lithium-ion full-cells employing TM co-doped SnO$_2$ as anode and a theoretical LiNi$_{0.5}$Mn$_{1.5}$O$_4$ (LNMO) cathode with a working voltage 4.7 V vs. Li/Li$^+$ and a specific capacity of 140 mAh g^{-1} (the energy density values reported herein are based on the mass of the anode and cathode active material; the N:P ratio was assumed to be 1).

The comparison of the XRD data recorded for carbon-coated and non-coated SnO₂ shows that the crystalline structure is generally well maintained apart from a minor reduction to metallic tin (Figure S5). Similarly, the comparison of carbon-coated and non-coated SCMO reveals that the structure is, in general, well preserved (Figure 4a). At around 47/48°, though, a very low intensity additional reflection is observed that may correspond to a SnCo alloy and/or some manganese oxide (indicated by an asterisk in Figure 4a) –both showing the main reflection in this 2θ region. As there are no other additional reflections observed, it appears difficult to differentiate between these two phases, which both might result from some minor reduction of the original SCMO phase. In fact, this finding allows for two conclusions: (i) the confirmation that the two dopants are well introduced into the crystalline stannite lattice and (ii) the indication that the TM doping enhances the thermal stability of the oxide phase under a reducing atmosphere, as the reflection/s is/are less in intensity, broader, and simply less than for pristine SnO₂, while the formation of some SnCo alloy phase and manganese oxide might, indeed, be the thermodynamically most favored phases under such conditions. This minor reduction, however, does not have any significant impact on the particle morphology, which is well maintained, as confirmed by TEM analysis (Figure 4b), while the carbon forms a homogeneous layer around the secondary particles, additionally electronically interconnecting the primary, nanorod-shaped SCMO@C particles.

Comparing initially the dis-/charge profile for the first and second galvanostatic cycle of SnO₂ and SnO₂@C (Figure S6a) reveals that the two profiles are largely overlapping. Nonetheless, there are also some important differences. For the first cycle (Figure S6a), the lithiation follows essentially the same voltage profile and also upon delithiation the two curves are initially overlapping almost perfectly. The major deviation occurs at about 2.0 V, above which SnO₂ shows a sharp increase in voltage, while SnO₂@C reveals a continuously sloped change and further capacity at such high potentials, indicating the enhanced reversibility of the conversion reaction thanks to the

presence of the electron-conducting carbon coating. Apparently, the application of the carbon coating has a similar effect as the incorporation the TM dopant(s). For the second cycle (Figure S6b), this difference for the delithiation process is maintained and getting even more pronounced, confirming a better reversibility of the conversion reaction thanks to the carbon coating. In addition, the shape of the lithiation profile reveals some difference for the two samples: SnO₂@C shows a rather steep decrease in voltage until about 1.6 V at which the slope decreases before it decreases again at about 0.5 V. Differently, SnO₂ shows an even steeper drop in voltage until about 1.25 V, followed by slight increase and immediate decrease in voltage which is commonly assigned to the nucleation barrier for the forthcoming conversion reaction to metallic tin and lithium oxide.[22] Subsequently, the two profiles are basically following the same behavior until the lower cut-off potential of 0.01 V is reached.

To further investigate the impact of the two different approaches, i.e., the application of a carbon coating vs. the introduction of the TM dopants, we performed a comparative electrochemical characterization of SCMO, SCMO@C, and SnO₂@C (Figure 5). The constant current cycling at 0.1 A g⁻¹ with an anodic cut-off potential of 3.0 V reveals substantially enhanced cycling stability for SCMO@C relative to both SCMO and SnO₂@C (Figure 5a), providing a specific capacity of 1090 mAh g⁻¹ after 50 cycles, which corresponds to a capacity retention of 87% (compared to only 28% for SCMO and 38% for SnO₂@C). Apparently, the combination of both approaches, i.e., TM co-doping and carbon coating is highly complementary. Similarly, the rate performance of SCMO@C is far superior to the other two active materials (Figure 5b–d) independent of the anodic cut-off potential, while the TM co-doping appears superior for the rate capability compared to the carbon coating (see also Table S1). In fact, also for the long-term cycling stability, the TM co-doping is more beneficial than the application of the carbon coating when decreasing the anodic cut-off from 3.0 V (SnO₂@C > SCMO; Figure 5b) to 2.0 V
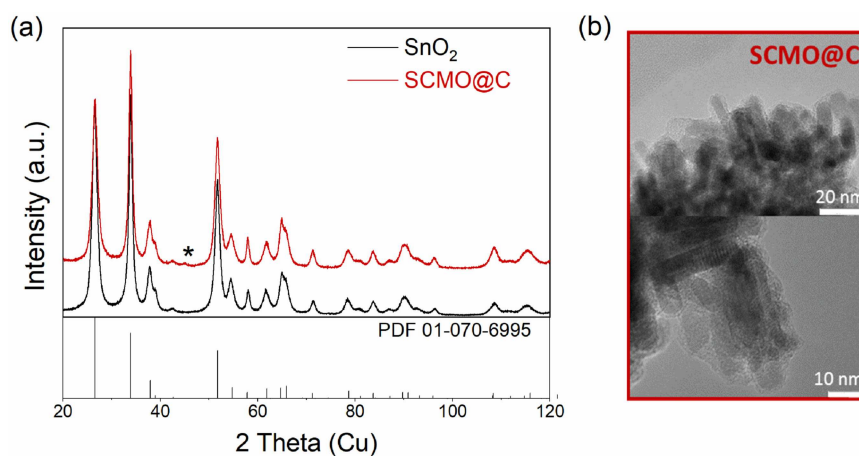

Figure 4. (a) Comparison of the XRD patterns of as-synthesized SCMO and carbon-coated SCMO@C. (b) TEM micrographs of SCMO@C at two different magnifications. The asterisk indicates a minor phase impurity observed after applying the carbon coating, which might correspond to a SnCo alloy and/or manganese oxide species.
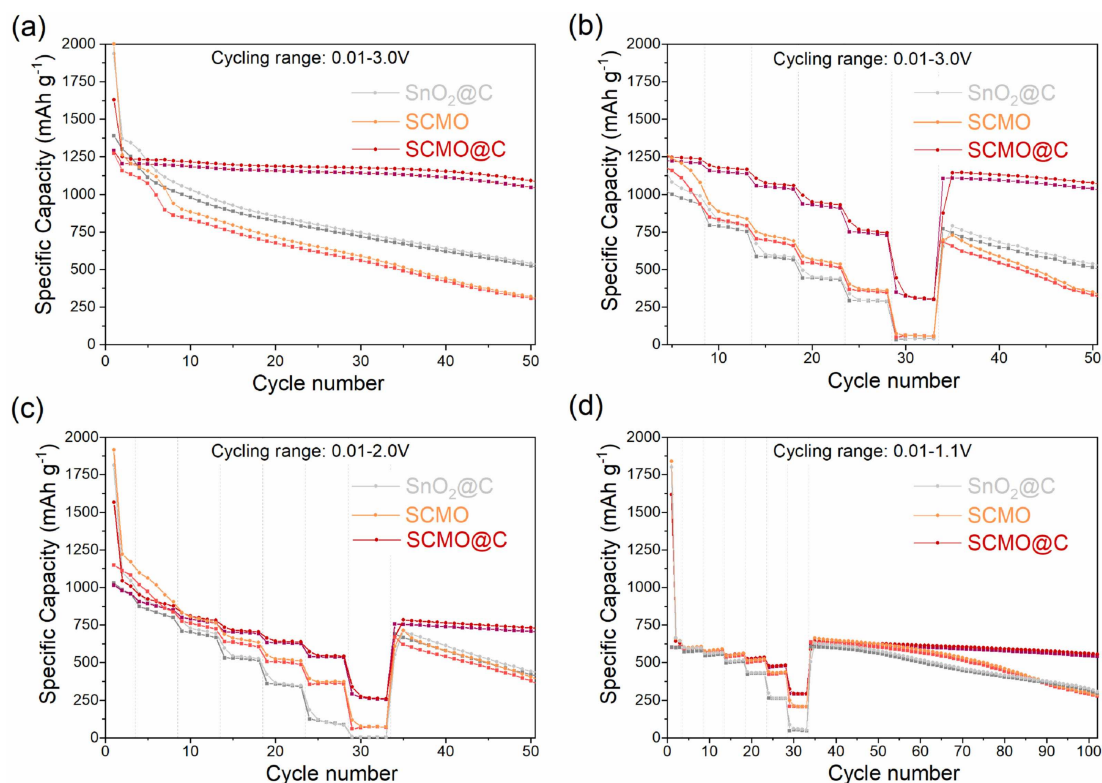
Figure 5. Comparison of the electrochemical performance for electrodes based on as-synthesized SCMO, carbon-coated SnO₂@C and SCMO@C by means of (a) constant current cycling at 0.1 A g⁻¹ and (b–d) applying elevated specific currents, setting the anodic cut-off potential to (b) 3.0 V, (c) 2.0 V, and (d) 1.1 V. Note that for (b) in case of SCMO, the cell was cycled only once at C/20 instead of thrice as for SCMO@C and SnO₂@C.

(SnO₂@C ≈ SCMO; Figure 5c) and, eventually, to 1.1 V (SnO₂@C < SCMO; Figure 5d).

These results further highlight (i) the advantageous complementarity of the two approaches and (ii) the superior impact of the transition metal doping over the carbon coating, as also reflected by the substantially decreased 1st cycle irreversibility, which generally follows the trend SCMO > SnO₂@C > SCMO@C (i.e., 36%, 29%, and 21%, respectively). Besides, the variation of the anodic cut-off potential underlines the importance of limiting the delithiation–which is, in fact, not only beneficial for the eventually achievable energy density on the full-cell level (as discussed earlier), but moreover reasonable for any practical application of these materials. Like this, SCMO@C shows a capacity retention of 90% after 100 cycles at various C rates compared to only 48% for SCMO and 52% for SnO₂@C.

2.4. Realization of SCMO-C/LNMO Li-Ion Full-Cells

Finally, to support the earlier conducted theoretical calculation for the full-cell energy density, we combined SCMO@C as negative electrode active material with high-voltage LNMO-based positive electrodes to obtain lithium-ion full-cells. In fact, apart from a very recent study by Wu et al.[23] who coupled a composite of hollow SnO₂ nanospheres, nitrogen-doped carbon, and graphene with LiCoO₂ cathodes, obtaining a capacity retention of about 60% after 90 cycles, this is one of the first

studies on such full-cells – to the best of our knowledge – and the first one comprising high-voltage LNMO as positive electrode active material (as well as TM-doped SnO₂ for the negative electrode). To rule out the impact of the large initial irreversibility of the anode, it was discharged first in half-cell configuration and recharged to an upper cut-off voltage of 1.1 V prior to the full-cell assembly.

Figure 6a depicts the deconvolution of the anode, cathode, and full-cell voltage profiles; the latter being simply the sum of the two single electrodes. The LNMO cathode shows the characteristic voltage profile with a long plateau at about 4.7 V upon charge and discharge. Also the anode reveals the characteristic charge (i.e., lithiation) profile, while the discharge (i.e., delithiation) profile shows some peculiar feature towards the end. The voltage is slightly decreasing and then increasing again at elevated voltages. This behavior is maintained also for the subsequent cycles (Figure 6b) and assigned to some manganese dissolution from the cathode which migrates to the anode and get reversibly oxidized and reduced there at about 2.0 V.[24–26] As such transition metal dissolution is considered inferior for the long-term cycling stability, future efforts will have to be dedicated to avoiding this issue, e.g., by protecting the LNMO particles from direct contact with the electrolyte. Besides, however, the evolution of the voltage profiles is rather stable apart from the moderate increase of the upper cut-off voltage of the SCMO@C anode, which has been observed earlier also for full-cells comprising carbon-coated ZnFe₂O₄ and
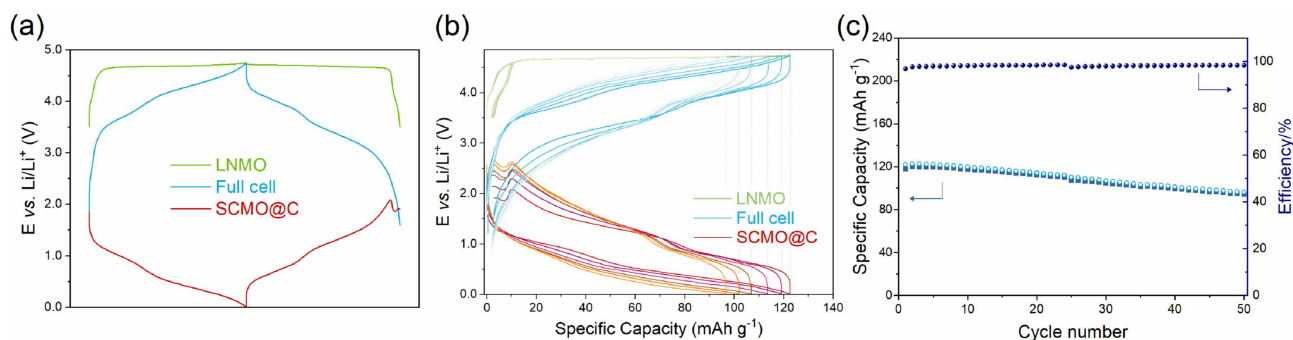
Figure 6. Electrochemical characterization of SCMO@C/LNMO lithium-ion full-cells via galvanostatic cycling: (a) Separation of the voltage profiles of the LNMO cathode (green), the SCMO@C anode (dark red), and the full-cell (blue) for the 3rd cycle; (b) Evolution of the separated voltage profiles, exemplarily presented for the 2nd, 10th, 20th, 30th, 40th, and 50th cycle; (c) Plot of the specific capacity and coulombic efficiency vs. the cycle number. All capacity values refer to the active material mass loading of the LNMO cathode and the SCMO@C anode was prelithiated as detailed in the experimental section.

attributed to the stepwise consumption of the lithium reservoir.[27] The LNMO cathode, indeed, is not affected by any change in voltage and the minor capacity fading from the initial >120 mAh g^{-1} occurs along the voltage plateau. Generally, though, the capacity retention is rather stable considering the non-optimized balancing (here, an N:P ratio of ca. 2 was used), as also apparent from the capacity vs. cycle number plot provided in Figure 6c. The capacity retention after 50 cycles is 81%, which is very promising for future studies. The specific energy (based on the anode and cathode active material) is 312 Wh kg^{-1} for the 3rd cycle, accompanied by an energy efficiency of remarkable 86%. Such specific energy is superior to a comparable graphite/LNMO full-cell with 259 Wh kg^{-1},[28] while the energy efficiency is slightly lower compared to the latter system (above 90%) – though in the same range as for lithium-ion full-cells comprising a silicon/carbon composite as anode and LNMO as cathode.[29] Upon cycling, however, the energy efficiency decreases to 74% in the 50th cycle, which is in line with the moderate increase in voltage hysteresis observed in Figure 6b for the anode. The value for the specific energy obtained experimentally is somewhat lower than the theoretical calculation presented in Figure 3b. Nonetheless, it has to be kept in mind that the LNMO capacity assumed in that calculation has been 140 mAh g^{-1}, which is significantly higher (ca. 13%) than the capacity provided by the LNMO positive electrodes used for this lithium-ion full-cell. Moreover, when adjusting the N:P ratio to a commonly employed value of 1.1 in commercial cells[30] (or even lower as done for the theoretical calculation to highlight the maximum possible), the specific energy would increase to 358 Wh kg^{-1} (and more, depending on the eventual ratio, and not including, yet, any potentially higher capacity for the cathode). Keeping these factors in mind – together with an optimized utilization of the anode in order to limit the upper cut-off to, e.g., 1.1 V renders these results very stimulating for further optimization.

3. Conclusions

A continuous hydrothermal flow synthesis method (CHFS) was shown to be a suitable route to successfully and directly prepare phase-pure SnO$_2$ nanoparticles incorporating at least three TM dopants. These active materials revealed enhanced electrochemical performances compared to pure SnO$_2$ due to the synergistic effect of the different TM dopants, which allowed for tailoring the dis-/charge redox potentials and, thus, eventually also improved energy densities on the full-cell level. In particular, the combination of manganese and cobalt outperformed the other TM co-doped tin oxides; the Mn lowered the average delithiation potential and enhanced rate capability (at lower anodic cut-off potentials) and cobalt enhanced the reversible capacities. The additional application of a carbonaceous coating further improved the cycling stability (effectively independent of the upper cut-off potential) and greatly enhanced the rate capability, while the impact of the TM co-doping is more effective in improving the performance as the carbon coating only. As a result, carbon-coated SCMO@C displayed a capacity retention of 90% after 100 cycles with a delithiation cut-off potential of 1.1 V, which is far superior to the comparatively investigated SCMO and SnO$_2$@C. To complete our study and support the earlier findings, the high-voltage SCMO@C/LNMO full-cells were prepared, demonstrating stable cycling and suitable gravimetric energy densities – given the constraints discussed. Overall, this study has revealed that carefully selected TM dopants have a dramatic impact on the performance of tin oxide anodes and it is anticipated that this work will pave the way for the development of further optimized high-energy and high-power conversion/alloying-type anode materials for LIBs in the future.

Experimental Section

Material Synthesis

The CHFS process is shown in a simplified flow diagram in Figure 1a. To summarize the process, three diaphragm pumps

(Primeroyal K, Milton Roy, Pont-Saint-Pierre, France) were used to supply feeds of deionized water (*via* pump P_{sw}), an aqueous solution of the transition metal (TM) dopant metal salts (*via* pump $P_{M(NO3)x}$), and an aqueous solution of potassium stannate trihydrate (*via* pump P_{K2SnO3}) at flow rates of 80, 40, and 40 mL min^{-1}, respectively. The metal salts used were potassium stannate trihydrate (99%, Sigma Aldrich, Dorset, U.K.), cobalt (II) nitrate hexahydrate (99%, Sigma Aldrich, Dorset, U.K.), iron (III) nitrate nonahydrate (99%, Sigma Aldrich, Dorset, U.K.), and manganese (II) nitrate tetrahydrate (98%, Sigma Aldrich, Dorset, U.K.). In the CHFS process, the deionized water (DI) feed from pump P_{DI} was heated in flow to 450°C using a 7 kW custom-built in-line electrical heater. Separate precursor feeds from pumps $P_{M(NO3)x}$ and P_{K2SnO3}, with a total metal concentration of 0.5 M, were first mixed in a T-piece in flow (at room temperature) prior to mixing in flow with the superheated water feed in the patented confined jet mixer (CJM).[31] A summary of the exact precursor concentrations used for each sample can be found in Table S2. Upon formation of the nanoparticles in the CJM, the hot particle-laden flow was then cooled in the CHFS process to ~40°C using a 1.5 m long counter-current pipe-in-pipe heat exchanger, before the slurry passed through a back-pressure regulator (BPR) valve. The aqueous nanoparticle slurry exiting the BPR was collected and cleaned by dialysis in DI water until the conductivity of the supernatant was consistently below 50 µS, as measured by a conductivity probe (Hanna Instruments, model HI98311, Leighton Buzzard, UK). The resulting concentrated slurry (using centrifugation) was then freeze-dried (Virtis Genesis 35XL) by gradually heating the samples from −60 to 25°C (over 24 h) *in vacuo* (< 100 mTorr), which yielded free-flowing powders.

Carbon Coating

A carbonaceous coating was applied to selected active materials in a separate step via a hydrothermal method. The active material was mixed with glucose in a ratio of 1:1.5, respectively, in DI water and magnetically stirred to obtain a homogeneous dispersion. Subsequently, the dispersion was transferred into a stainless steel autoclave (BERGHOF BR-100) and kept overnight at 180°C under vigorous stirring. After cooling to room temperature, the dispersion was centrifuged and the resulting precipitation was washed several times with deionized water and ethanol before being dried overnight at 80°C. Finally, the powder was thermally treated under argon atmosphere for 4 h at 500°C.

Morphological and Structural Characterization

All samples have been analyzed *via* powder X-ray diffraction (XRD, Bruker D8 Advance) with Cu-K$_\alpha$ radiation ($\lambda = 0.154$ nm). All diffractograms were recorded in the range of $2\theta = 20$–$120°$ with a step size of 0.02° and a counting time per step of 1.45 s. Transmission electron microscopy (TEM) (Philips CM 20, 200 kV) was conducted to obtain information about the particle size and morphology. Thermogravimetric analysis (TGA; TA Instruments Q5000) was performed with a heating rate of 3°C min^{-1} under O$_2$ atmosphere. The specific surface area was determined by means of nitrogen adsorption and calculated according to the Brunauer-Emmett-Teller (BET) theory using an Autosorb iQ from Quantachrome. Energy-dispersive X-ray spectroscopy (EDX) was performed on a Zeiss LEO 1550 microscope, equipped with an EDX spectrometer from Oxford Instruments (X-MaxN, 50 mm², 15 kV).

Electrochemical Characterization

The active materials used for the electrode processing were used without further treatment after the freeze-drying step (or after having applied the carbon coating). All electrodes were prepared by mixing 75 wt% of active material and 20 wt% of conductive carbon (SuperC65*, TIMCAL) with 5 wt% of sodium carboxymethyl cellulose (CMC, Dow Wolff Cellulosics) serving as binder. First, the CMC was dissolved in DI water. In a second step, the other components were added and finely dispersed using a planetary ball mill for about 2 h. Subsequently, the resulting slurry was cast on dendritic copper foil (Schlenk, 99.9%) using a doctor blade with a wet film thickness of 120 µm. The cast film was left overnight at room temperature for drying. Once dried, we punched disks with a diameter of 12 mm, which were subsequently dried in a Büchi oven for 12 h at 120°C under vacuum. The mass loading of the electrodes after drying is in the range of 1.5-2.0 mg cm^{-2}. For the electrochemical tests, we used both three-electrode and two-electrode cells. For the three-electrode cell configuration, Swagelok-type cells were used with lithium foil (Rockwood Lithium, battery grade) serving as counter ($\varnothing = 12$ mm) and reference electrodes. A GF/D Whatman glass fiber sheet, serving as separator ($\varnothing = 13$ mm), was soaked with the electrolyte, i.e., 1 M LiPF$_6$ in EC:DMC (1:1). For the two-electrode cells, 2032 coin cells (Hohsen) were used. Li foil served as counter (and internal reference) electrode ($\varnothing = 14$ mm), a sheet of GF/A Whatman glass fiber as separator ($\varnothing = 16$ mm), and a 1 M solution of LiPF$_6$ in EC:DEC (3:7) as electrolyte. According to some comparative tests, there was no significant impact of the given electrolyte composition on the electrochemical performance in half-cell configuration. All the cells have been prepared in an argon-filled glovebox (MBraun UNIlab with a H$_2$O and O$_2$ content of less than 0.01 ppm). For the full-cell characterization, LNMO electrodes were prepared as reported in Kuenzel *et al.*[32] and a three-electrode setup was used to deconvolute the voltage profiles of the anode and cathode using auxiliary channels with lithium metal foil as reference electrode. The electrolyte was 1 M LiPF$_6$ in EC:DMC (1:1), as this showed a better compatibility with the high-voltage cathode. Prior to the full-cell assembly, the anode was discharged to 0.01 V in half-cell configuration and recharged to 1.1 V in order to address the initial capacity loss and build up a certain lithium reservoir. Subsequently, the anode was recovered in the glove box and rinsed with DMC before coupling it with the LNMO cathode. All electrochemical studies were performed at 20°C±2°C. For the galvanostatic cycling of coin cells, a Maccor Battery Tester 4300 was utilized. Cyclic voltammetry experiments and galvanostatic cycling for the full cell were performed by means of a VMP3 potentiostat (BioLogic). Upon galvanostatic cycling of the full-cell, the operational potential window of the LNMO cathode and SCMO@C anode were limited to 4.8–3.5 V and 0.01–3.0 V vs. Li/Li$^+$, respectively. Hence, the maximum cell voltage was 4.79 V. Moreover, for the full-cell the dis-/charge rate was based on the cathode and 1 C corresponds to a specific current of 147 mAh g^{-1}.

[1] B. Scrosati, J. Garche, *J. Power Sources* **2010**, *195*, 2419.

[2] J. B. Goodenough, *Nat. Electron.* **2018**, *1*, 204.

[3] D. Bresser, K. Hosoi, D. Howell, H. Li, H. Zeisel, K. Amine, S. Passerini, *J. Power Sources* **2018**, *382*, 176.

[4] Y. Yamada, Y. Iriyama, T. Abe, Z. Ogumi, *Langmuir* **2009**, *25*, 12766.

[5] B. N. Loeffler, D. Bresser, S. Passerini, M. Copley, *Johns. Matthey Technol. Rev.* **2015**, *59*, 34.

[6] T. Waldmann, B.-I. Hogg, M. Wohlfahrt-Mehrens, *J. Power Sources* **2018**, *384*, 107.

[7] M. N. Obrovac, V. L. Chevrier, *Chem. Rev.* **2014**, *114*, 11444.

[8] P. Poizot, S. Laruelle, S. Grugeon, L. Dupont, J.-M. Tarascon, *Nature* **2000**, *407*, 496.

[9] M. R. Palacin, *Chem. Soc. Rev.* **2009**, *38*, 2565.

[10] N. Nitta, G. Yushin, *Part. Part. Syst. Charact.* **2014**, *31*, 317.

[11] D. Bresser, S. Passerini, B. Scrosati, *Energy Environ. Sci.* **2016**, *9*, 3348.

[12] F. Mueller, D. Bresser, V. S. K. Chakrayadhanula, S. Passerini, *J. Power Sources* **2015**, *299*, 398.

[13] M. Lübke, D. Ning, C. F. Armer, D. Howard, D. J. L. Brett, Z. Liu, J. A. Darr, *Electrochim. Acta* **2017**, *242*, 400.

[14] J. Wang, L. Wang, S. Zhang, S. Liang, X. Liang, H. Huang, W. Zhou, J. Guo, *J. Alloys Compd.* **2018**, *748*, 1013.

[15] Y. Ma, Y. Ma, U. Ulissi, Y. Ji, C. Streb, D. Bresser, S. Passerini, *Electrochim. Acta* **2018**, *277*, 100.

[16] Y. Ma, Y. Ma, G. Giuli, T. Diemant, R. J. Behm, D. Geiger, U. Kaiser, U. Ulissi, S. Passerini, D. Bresser, *Sustain. Energy Fuels* **2018**, *2*, 2601.

[17] F. Zoller, D. Böhm, T. Bein, D. Fattakhova-Rohlfing, *ChemSusChem* **2019**, *12*, 4140.

[18] R. Hu, Y. Ouyang, T. Liang, X. Tang, B. Yuan, J. Liu, L. Zhang, L. Yang, M. Zhu, *Energy Environ. Sci.* **2017**, *10*, 2017.

[19] T. Liang, R. Hu, H. Zhang, H. Zhang, H. Wang, Y. Ouyang, J. Liu, L. Yang, M. Zhu, *J. Mater. Chem. A* **2018**, *6*, 7206.

[20] J. A. Darr, J. Zhang, N. M. Makwana, X. Weng, *Chem. Rev.* **2017**, *117*, 11125.

[21] K. Xu, *Chem. Rev.* **2004**, *104*, 4303.

[22] R. A. Huggins, *Solid State Ionics* **1998**, *113–115*, 57.

[23] Q. Wu, Q. Shao, Q. Li, Q. Duan, Y. Li, H. Wang, *ACS Appl. Mater. Interfaces* **2018**, *10*, 15642.

[24] B. Aktekin, M. J. Lacey, T. Nordh, R. Younesi, C. Tengstedt, W. Zipprich, D. Brandell, K. Edström, *J. Phys. Chem. C* **2018**, *122*, 11234.

[25] C. Zhan, J. Lu, A. J. Kropf, T. Wu, A. N. Jansen, Y.-K. Sun, X. Qiu, K. Amine, *Nat. Commun.* **2013**, *4*, 2437.

[26] N. P. W. Pieczonka, Z. Liu, P. Lu, K. L. Olson, J. Moote, B. R. Powell, J.-H. Kim, *J. Phys. Chem. C* **2013**, *117*, 15947.

[27] A. Varzi, D. Bresser, J. von Zamory, F. Mueller, S. Passerini, *Adv. Energy Mater.* **2014**, *4*, 1400054.

[28] F. De Giorgio, N. Laszczynski, J. von Zamory, M. Mastragostino, C. Arbizzani, S. Passerini, *ChemSusChem* **2017**, *10*, 379.

[29] P. Meister, H. Jia, J. Li, R. Kloepsch, M. Winter, T. Placke, *Chem. Mater.* **2016**, *28*, 7203.

[30] J. Kasnatscheew, T. Placke, B. Streipert, S. Rothermel, R. Wagner, P. Meister, I. C. Laskovic, M. Winter, *J. Electrochem. Soc.* **2017**, *164*, A2479.

[31] J. A. Darr, C. J. Tighe, R. I. Gruar, *Co-Current Mixer, Apparatus, Reactor and Method for Precipitating Nanoparticles*, **2011**, WO2011148121A1.

[32] M. Kuenzel, D. Bresser, T. Diemant, D. Vieira Carvalho, G.-T. Kim, R. J. Behm, S. Passerini, *ChemSusChem* **2017**, *11*, 562.